RSC Advances

PAPER

View Article Online
View Journal | View Issue

Cite this: *RSC Adv.*, 2026, **16**, 25208

Strategic modular assembly of trifluoromethylated energetic materials *via* triazine-based scaffolds

Jiyuan Yu, Xiangyan Miao and Yuchuan Li *

Received 13th February 2026
Accepted 13th April 2026

DOI: 10.1039/d6ra01290f

rsc.li/rsc-advances

Nitrogen-rich frameworks with good thermal stability and low sensitivity have attracted considerable interest as potential energetic materials. Herein, a modular assembly strategy based on nucleophilic aromatic substitution (SNAr) on chloro-1,3,5-triazines was employed to construct triazine-bridged, CF_3-functionalized nitrogen-rich architectures, affording compounds **3** and **6**. Subsequent salt formation gave **4** and **5**, and the structures of **4** and **5** were confirmed by single-crystal X-ray diffraction. Among the compounds examined, **4** exhibits a relatively high density (ρ = 1.80 g cm^{-3}), improved detonation performance (D = 7664 m s^{-1}, P = 25.2 GPa), very low sensitivity (IS > 40 J, FS > 360 N), and good thermal stability (T_d,onset = 241.4 °C). These results show that triazine-based scaffold assembly combined with perchlorate modulation is a useful approach to tuning the balance among thermal stability, energetic performance, and low sensitivity in CF_3-containing nitrogen-rich systems.

Introduction

Energetic materials (EMs) are indispensable in explosives and propellants, where their practical use requires a delicate balance among detonation performance, thermal stability, and operational safety.[1] These materials are critically employed in defense, space exploration, and various civilian industries.[2,3] However, optimizing all key properties simultaneously is challenging, as improvements in one aspect often compromise another.[4] Representative examples of classical heat-resistant energetic compounds include 2,2′,4,4′,6,6′-hexanitrostilbene (HNS, T_d = 318 °C, D = 7612 m s^{-1}, P = 24.3 GPa) and 2,6-bis(picrylamino)-3,5-dinitropyridine (PYX, T_d = 360 °C, D = 7757 m s^{-1}, P = 25.1 GPa). However, their relatively high mechanical sensitivities (HNS: IS = 5 J, FS = 240 N; PYX: IS = 10 J, FS = 240 N) (Fig. 1) also illustrate the persistent trade-off between thermal robustness and safety.[5–7] Consequently, there remains an urgent need to develop EMs that are both thermally robust and significantly less sensitive.[8]

From a structural perspective, nitrogen-rich fused heterocycles paired with robust hydrogen-bond networks in the crystal lattice are highly favorable motifs for reducing mechanical sensitivity. These frameworks benefit from dense heteroatom arrays that support directional intermolecular contacts, thereby facilitating stress delocalization.[9,10] For example, TATOT (a 5/5-fused triazolo[4,3-*b*][1,2,4]triazole) exemplifies such a nitrogen-rich platform: it combines high intrinsic energy (Δ_fH = 446.7 kJ mol^{-1}; D = 9385 m s^{-1}; P = 29.7 GPa) with remarkably low sensitivity (IS = 40 J, FS = 360 N). This outstanding insensitivity is attributed to an extensive amino-driven hydrogen-bonding network in the crystal (Fig. 1).[11,12] However, all-amino fused systems are typically oxygen-deficient, indicating that additional design strategies are needed to maintain safety while further enhancing energetic output.[13]

In addition to fused-ring construction, incorporation of a CF_3 group is an effective means of improving energetic materials, particularly by increasing density and lowering mechanical sensitivity.[14,15] Previous studies have shown that CF_3-containing nitrogen-rich fused frameworks can combine low sensitivity with relatively high density and useful detonation performance. For example, precursor **2**, 6-(trifluoromethyl)-7*H*-[1,2,4]tri-azolo[4,3-*b*][1,2,4]triazole-3,7-diamine, exhibits a density of 1.82 g cm^{-3}, a detonation velocity of 7706 m s^{-1}, and a detonation pressure of 21.7 GPa, while maintaining low

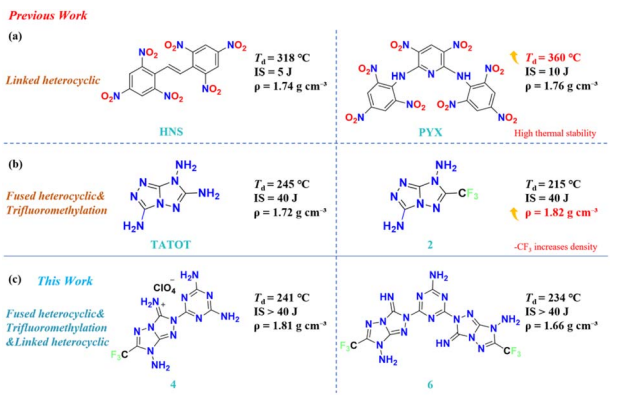

Fig. 1 (a) N-heterocycle bridging for enhanced thermal stability. (b) CF_3 functionalization for increased density. (c) This work.

School of Materials Science & Engineering, Beijing Institute of Technology, Beijing 100081, China

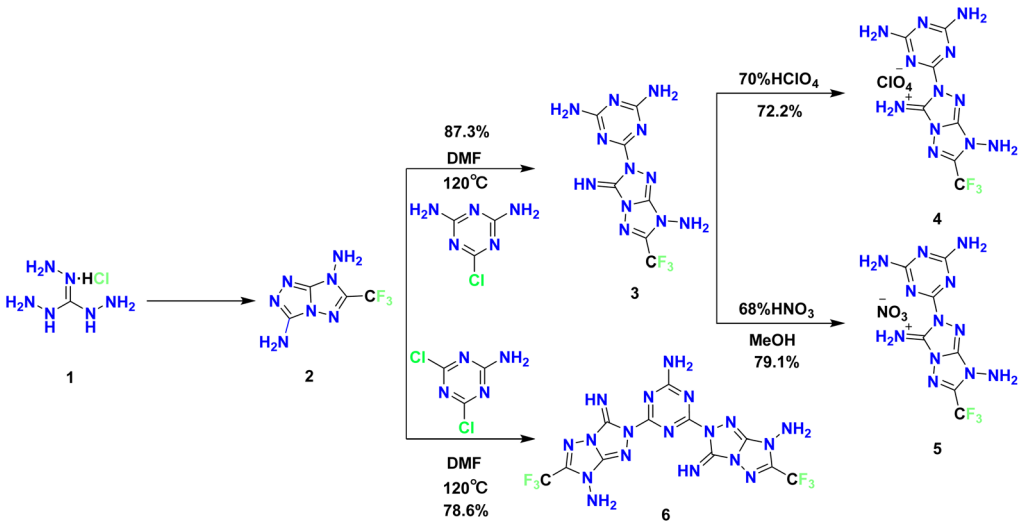

Scheme 1 Synthesis of energetic molecules **3**–**6**.

sensitivity (IS = 40 J, FS = 360 N).[16] Fluorinated frameworks are also of interest for aluminium-containing energetic systems because fluorine-containing species can promote surface alumina conversion and facilitate aluminium ignition and combustion.[17] Nevertheless, the intrinsic oxygen deficiency of CF_3-containing scaffolds limits further improvement in energetic output and therefore calls for complementary structural regulation.

Among the available molecular design strategies for next-generation EMs, the electron-deficient 1,3,5-triazine ring is an attractive motif because it enables modular assembly *via* SNAr reactions and can reorganise intermolecular interactions in the solid state.[18,19] Previous studies have shown that fusion of a triazine unit into a nitrogen-rich framework, followed by perchlorate formation, can improve thermal stability and sensitivity. For example, 2,4,7-triamino-8-nitropyrazolo[1,5-*a*][1,3,5]triazin-1-ium perchlorate exhibits a higher onset decomposition temperature than its precursor 3,5-diamino-4-nitro-1*H*-pyrazol-2-ium perchlorate (279 *vs.* 194 °C), while the impact and friction sensitivities are reduced from 5 J and 160 N to 40 J and 240 N, respectively.[20] These results indicate that the combination of triazine incorporation and oxygen-rich counteranion modulation is a viable strategy for optimising the overall behaviour of nitrogen-rich energetic frameworks.[21]

On this basis, we sought to integrate a CF_3-functionalised fused precursor with a chlorotriazine platform through a triazine-based SNAr strategy. In this work, neutral triazine-bridged frameworks **3** and **6** were constructed from precursor **2**, and **3** was further converted into salts **4** and **5** through ionic modulation with perchlorate and nitrate. This design was intended to compensate for the oxygen deficiency of the CF_3-containing scaffold and to tune density, decomposition behaviour, detonation performance, and mechanical sensitivity within a single modular platform.[22,23] In particular, perchlorate salt **4** retains low sensitivity while increasing the density from 1.71 to 1.80 g cm^{-3} and improving detonation performance from 6994 m s^{-1}/19.3 GPa to 7664 m s^{-1}/25.2 GPa, indicating that this strategy is useful for improving the overall property balance of this CF_3-containing energetic system.

Results and discussion

Synthesis

As shown in Scheme 1, precursor **2**, prepared according to the reported procedure,[24] reacted with 2-chloro-4,6-diamino-1,3,5-triazine to afford **3** in 87.3% isolated yield, whereas coupling with 4,6-dichloro-1,3,5-triazine-2-amine gave **6** in 78.6% yield. Subsequent salt formation of **3** with perchloric acid and nitric acid furnished **4** and **5** in 72.2% and 79.1% yields, respectively. These results indicate that the present triazine-based SNAr strategy proceeds efficiently under straightforward experimental conditions. It should be noted that the single crystals of **4**·H_2O and **5**·$5H_2O$ were obtained from aqueous recrystallization for X-ray diffraction analysis only. In contrast, the bulk samples used for DSC measurements, density determination, sensitivity testing, and energetic calculations were isolated as solid powders from synthesis, washed with acetonitrile, and dried prior to use. Therefore, the hydrated crystal compositions observed in the single-crystal structures do not necessarily represent the state of the bulk samples employed in the physicochemical measurements discussed below.

X-ray crystallographic analysis

Compound **4**·H_2O (CCDC: 2525729) crystallizes in the triclinic crystal system with the $P\bar{1}$ space group (Fig. 2). The unit–cell parameters are $a = 13.619(2)$ Å, $b = 15.295(3)$ Å, $c = 17.404(2)$ Å, $\alpha = 69.224(6)°$, $\beta = 69.711(6)°$, and $\gamma = 83.327(7)°$, giving a cell volume of 3179.2(9) $Å^3$ with $Z = 2$. The calculated crystal density is 1.757 g cm^{-3} at 170 K. The asymmetric unit comprises a protonated cation, perchlorate counterions, and lattice solvent/water species modelled over disordered sites. In the solid state, extensive intermolecular N–H···O hydrogen bonds

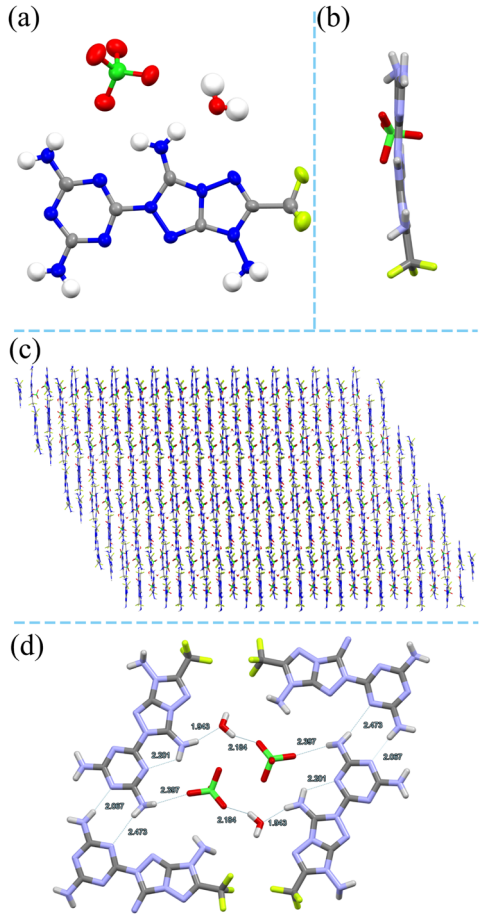

Fig. 2 (a) Crystal structure of $4\cdot H_2O$; (b) side view for $4\cdot H_2O$ (water molecule is omitted for better clarity); (c) perspective view of $4\cdot H_2O$; (d) hydrogen-bonding interactions in the crystal of $4\cdot H_2O$.

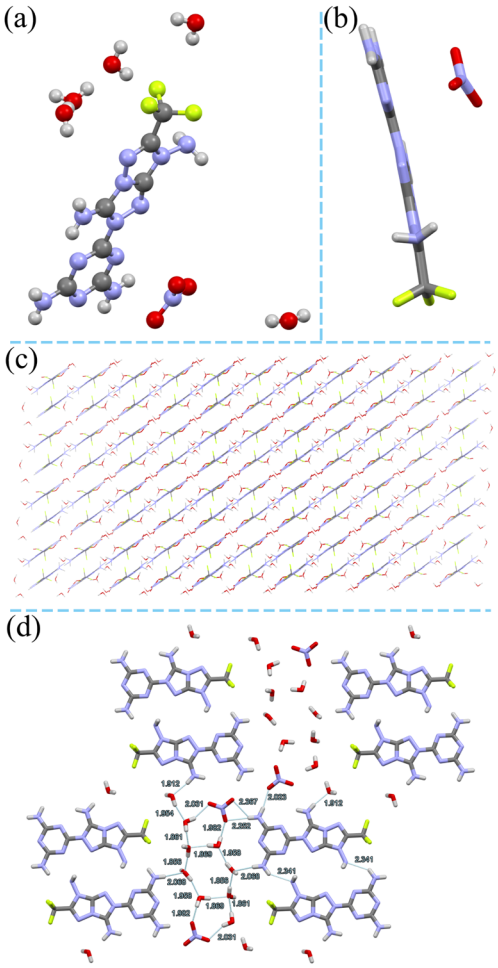

Fig. 3 (a) Crystal structure of $5\cdot 5H_2O$; (b) side view for $5\cdot 5H_2O$ (water molecule is omitted for better clarity); (c) perspective view of $5\cdot 5H_2O$. (d) Hydrogen-bonding interactions in the crystal of $5\cdot 5H_2O$.

between amino/imino donors and perchlorate oxygen atoms (H···O = 1.94–2.53 Å; N···O = 2.80–3.28 Å), together with N–H···N contacts among neighbouring nitrogen-rich heterocycles (H···N = 2.09–2.43 Å), connect the ionic components into a robust three-dimensional hydrogen-bonded network.

Compound $5\cdot 5H_2O$ (CCDC: 2530986) crystallizes in the triclinic crystal system with the $P\bar{1}$ space group (Fig. 3). The calculated crystal density is 1.632 g cm^{-3} at 100 K. The asymmetric unit contains a protonated cation, one nitrate anion, and five lattice water molecules. The cation adopts an almost planar conformation, which is further stabilized by an intramolecular N–H···N contact (N18–H18B···N15, N···N = 2.770 Å). In the crystal, the amino group donates a bifurcated hydrogen bond to the nitrate oxygen atoms (N16–H16A···O25/O26, D···A = 3.128/2.991 Å), thereby anchoring the anion adjacent to the cation. Meanwhile, the lattice water molecules are linked through short O–H···O hydrogen bonds (O···O = 2.723–2.803 Å) to generate an extended hydration network that bridges the ionic components. As a result, the packing is governed predominantly by hydrogen-bonding interactions, while neighbouring π-surfaces are separated by the hydrated nitrate/water units rather than by pronounced face-to-face π–π stacking.

Thermal properties

The thermal behavior of compounds **3–6** was investigated by DSC under N_2 at heating rates of 5, 10, 15, and 20 °C min^{-1} (Fig. 4). All four compounds showed a dominant exothermic decomposition event, with T_p shifting to higher temperature as the heating rate increased. No distinct low-temperature endothermic signal attributable to dehydration was observed for the measured bulk samples, suggesting that these powders did not retain the same hydrated state as the recrystallized single-crystal hydrates. At 10 °C min^{-1}, compound **3** exhibited the highest T_{onset} (254 °C; T_p = 257 °C), whereas salts **4** and **5** showed earlier onsets (T_{onset} = 241 °C for both) but similar T_p values (258 and 257 °C, respectively). Compound **6** displayed the lowest thermal stability, with T_{onset} = 234 °C and T_p = 237 °C. In addition, ΔT values for **4** and **5** were much larger than those for **3** and **6**, indicating a more gradual initial decomposition process in the salt forms. Compared with precursor **2** (T_{onset} = 215 °C), compounds **3–6** show improved decomposition thresholds, indicating that incorporation of the triazine unit enhances thermal resistance within this CF_3-containing fused

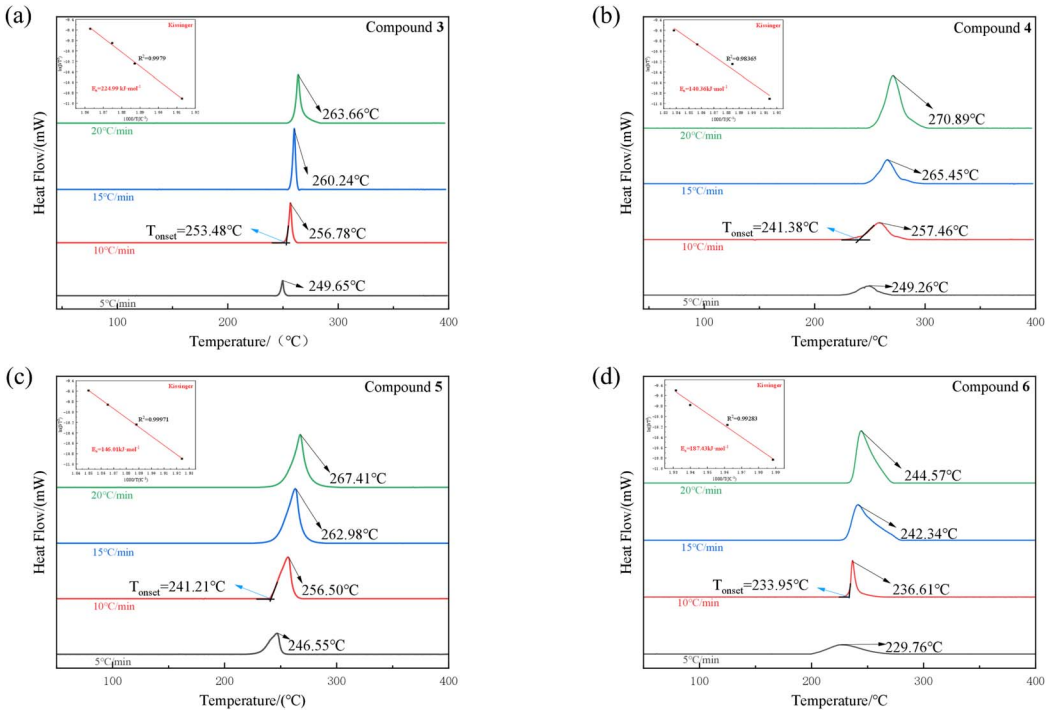

Fig. 4 DSC curves (different heating rates) and Kissinger curves of (a) compound **3**, (b) compound **4**, (c) compound **5** and (d) compound **6**.

framework, whereas salt formation mainly modifies the onset behavior rather than further increasing T_{onset}.

Kinetic analysis. To quantify the decomposition kinetics, the apparent activation energies (E_a) were determined using non-isothermal methods according to the following equations:[25,26]

$$\ln\left(\frac{\beta}{T_p^2}\right) = \ln\frac{AR}{E_a} - \frac{E_a}{RT_p} \quad (1)$$

$$\ln\ \beta = \lg\left(\frac{AE_a}{Rg(\alpha)}\right) - 2.315 - 0.4567\frac{E_a}{RT_p} \quad (2)$$

Ozawa plots of $\log\beta$ *versus* $1000/T_p$ yielded excellent linearity ($R^2 \geq 0.98$), affording E_a values of 222.3 kJ mol^{-1} for **3**, 141.9 kJ mol^{-1} for **4**, 147.22 kJ mol^{-1} for **5**, and 186.3 kJ mol^{-1} for **6** (Fig. S19–S22). These values are in close agreement with those obtained from Kissinger's method (224.99, 140.36, 146.01, and 187.43 kJ mol^{-1} for **3**, **4**, **5** and **6**, respectively), confirming the reliability of the kinetic analysis. The trend in decomposition barriers (**3** > **6** > **5** > **4**) parallels the order of their onset temperatures, indicating that incorporation of oxygen-containing counter-anions *via* salt formation markedly lowers the activation energy (by ~75–80 kJ mol^{-1} relative to **3**) while maintaining a similar T_p at 10 °C min^{-1} for the salts (T_p = 257.46 °C for **4** and 256.50 °C for **5**, *versus* 256.78 °C for **3**). Overall, compound **3** exhibits the highest thermal decomposition barrier, followed by the dimer **6**, whereas the ionic salts **4** and **5** show substantially reduced E_a values, consistent with their facilitated initial decomposition. This hierarchy reflects how salt formation modulates the decomposition kinetics: the ionic salt **4**/**5** initiates decomposition more readily than neutral **3**, yet still achieves a peak decomposition temperature on par with **3**. These results indicate that targeted structural modifications can preserve thermal stability while adjusting decomposition kinetics, which is critical for designing next-generation insensitive energetic materials.

Energy and sensitivity properties

The energetic performance of compounds **3–6** was evaluated using Explo5 (v6.01)[27] based on their heats of formation (Δ_fH), obtained from quantum-chemical calculations (Gaussian 09, Tables S8 and S9), and experimentally measured densities (ρ).[28] The density values used for these evaluations were 1.71, 1.80, 1.78, and 1.66 g cm^{-3} for compounds **3**, **4**, **5**, and **6**, respectively. For compounds **4** and **5**, these physicochemical data correspond to the bulk samples used for the measurements rather than to the hydrated single-crystal forms obtained from aqueousrecrystallization. The calculated Δ_fH values are −5.73 kJ mol^{-1} for **3**, +13.67 kJ mol^{-1} for **4**, −619.5 kJ mol^{-1} for **5**, and +20.8 kJ mol^{-1} for **6**. For comparison of thermal stability, T_d is defined here as the onset decomposition temperature (T_{onset}) measured by DSC at 10 °C min^{-1} under N_2, giving values of 253 °C (**3**), DSC at 10 °C min^{-1} under N_2, giving values of 253 °C (**3**), 241 °C (**4**), 241 °C (**5**), and 234 °C (**6**). As shown in Table 1, the neutral compounds **3** and **6** exhibit moderate detonation performance, with *D*/*P* values of 6994 m s^{-1}/19.3 GPa and 6812 m s^{-1}/19.2 GPa, respectively, which are close to those of TNT (7303 m s^{-1} and 21.3 GPa). Although compound **6** has a higher positive Δ_fH than **3**, its lower density results in slightly reduced detonation output. In contrast, conversion of **3** into the perchlorate salt **4** leads to

Table 1 Physicochemical and energetic properties of compounds **3–6**

Compd	T_d[a] (°C)	D_v[b] (m s^{-1})	P[c] (GPa)	$\Delta_f H$[d] (kJ mol^{-1})	IS[e] (J)	FS[f] (N)	ρ[g] (g cm^{-3})
2	215	7706	21.7	−193.5	40	360	1.82
3	253	6994	19.3	−5.7	>40	>360	1.71
4	241	7664	25.2	13.7	>40	>360	1.80
5	241	7228	20.8	−619.5	>40	>360	1.78
6	234	6812	19.2	20.8	>40	>360	1.66
TATOT	245	9385	29.7	446.7	40	360	1.72
HNS	318	7612	24.3	78.2	5	240	1.74
PYX	360	7757	25.1	−11.6	10	240	1.76
TNT[h]	295	7303	21.3	−59.3	15	353	1.65

[a] Densities, sensitivities and energetic calculations for **3–6** correspond to the dried bulk samples. Thermal decomposition temperature (onset) under nitrogen gas (DSC, 10 °C min^{-1}). [b] Calculated detonation velocity (calculated with Explo5 6.01). [c] Calculated detonation pressure (calculated with Explo5 6.01). [d] Calculated heat of formation. [e] Impact sensitivity. [f] Friction sensitivity. [g] Measured densities, gas pycnometer at room temperature. [h] Ref. 29.

a marked increase in density (1.71 → 1.80 g cm^{-3}) and a corresponding enhancement in detonation performance (D = 7664 m s^{-1}, P = 25.2 GPa). These values approach those of HNS (7612 m s^{-1}, 24.3 GPa) and PYX (7757 m s^{-1}, 25.1 GPa), although compound **4** still decomposes at a lower onset temperature than these classical thermostable explosives. The nitrate salt **5** also shows a density increase relative to **3** (1.78 g cm^{-3}) and exhibits intermediate performance (D = 7228 m s^{-1}, P = 20.8 GPa), lying between neutral **3** and perchlorate salt **4**.

Mechanical sensitivity measurements further show that all four compounds are consistently insensitive toward external stimuli, with impact sensitivities above 40 J and friction sensitivities above 360 N. These values are significantly lower than those of HNS, PYX, and TNT, indicating that low mechanical sensitivity is a common feature across this series. Taken together, these results suggest that ionic modulation through salt formation can effectively tune density and detonation output within this CF_3-containing, nitrogen-rich framework while preserving very low mechanical sensitivity. Among the compounds examined here, perchlorate salt **4** provides the most balanced combination of detonation performance and insensitivity, whereas compound **3** retains the highest resistance to initial thermal decomposition.

Structure–property relationship

To rationalize the low mechanical sensitivities (IS > 40 J, FS > 360 N) and the distinct thermal-decomposition behaviors of **3**, **[3H]**$^+$ and **6**, electrostatic potential (ESP)[30,31] analyses were performed for **3** and **[3H]**$^+$, and a Hirshfeld surface (HS)[32] analysis was applied to **[3H]**$^+$ based on its single-crystal structure. Since suitable single crystals of **3** were not obtained, HS descriptors could not be calculated for the neutral precursor. For the ionic salt **4**, the HS analysis was carried out on the basis of its crystallographically characterized protonated cation-perchlorate assembly. Nevertheless, the combined HS and ESP results provide a consistent picture of how salt formation reshapes the intermolecular contact network and the surface charge landscape.

For **4**, the HS mapped with *d*_norm (Fig. 5) displays pronounced close-contact features around the protonated N–H donors and the oxygen-rich ClO_4^- acceptors, indicating strong and highly directional N–H···O interactions. Quantitatively, the 2D fingerprint plots reveal that hydrogen-bond-related contacts dominate lattice cohesion: N···H/H···N contacts account for 15.6% and O···H/H···O contacts for 13.8%, together contributing 29.4% of the total surface contacts. In addition, H···H

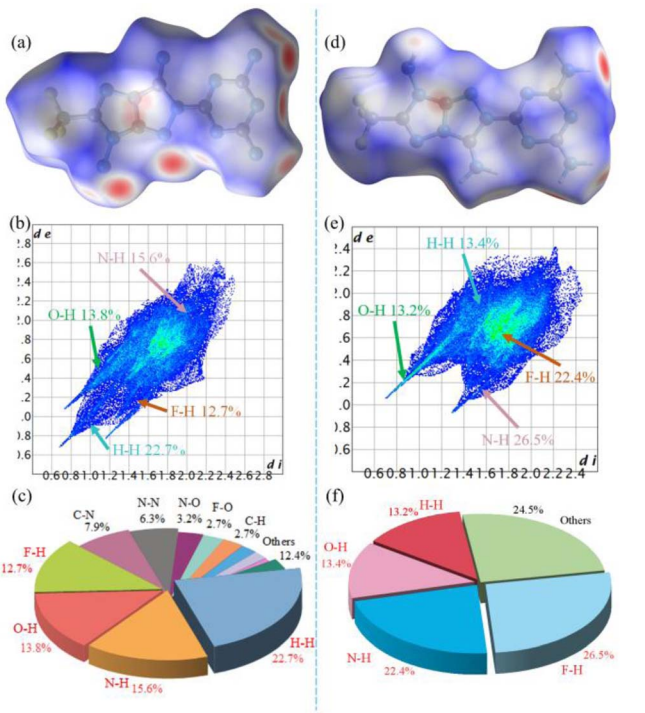

Fig. 5 (a) Hirshfeld surface of **4** mapped over d_norm showing short contacts; (b) 2D fingerprint plots for **4** indicating the contributions of different contact types; (c) pie chart of the percentage contributions of individual atomic contacts to the Hirshfeld surface of **4**; (d) Hirshfeld surface of **5** mapped over *d*_norm showing short contacts; (e) 2D fingerprint plots for **5** indicating the contributions of different contact types; (f) pie chart of the percentage contributions of individual atomic contacts to the Hirshfeld surface of **5**.

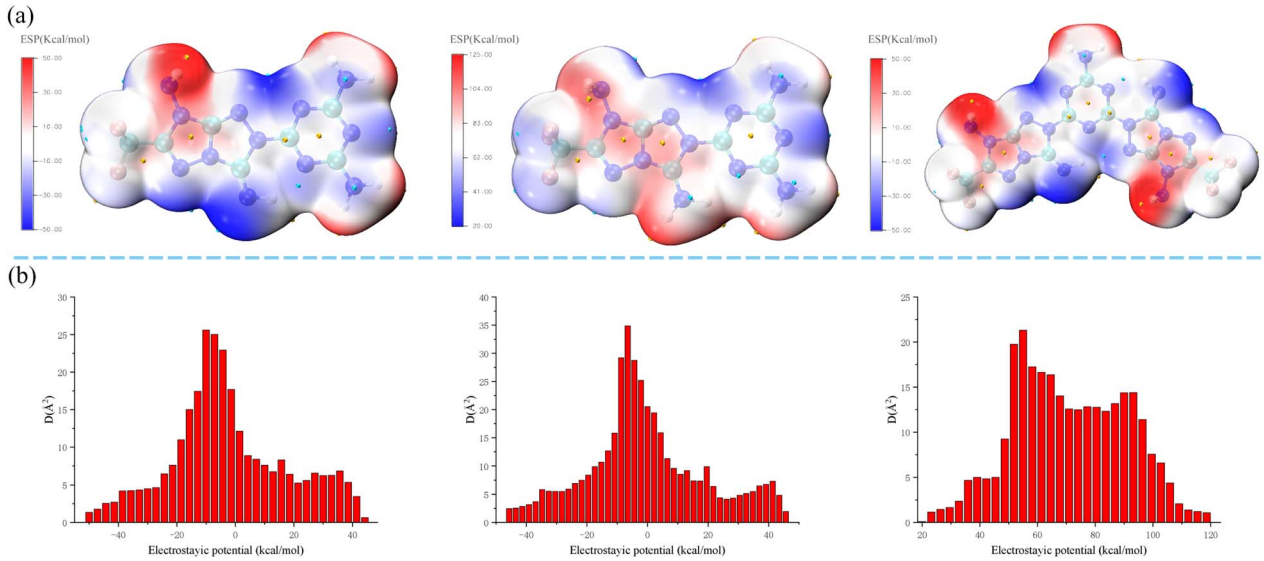

Fig. 6 (a) Electrostatic potential (ESP) maps of **3**, the protonated cation **[3H]**$^+$ derived from **4**, and **6**; (b) corresponding ESP distributions shown as bar graphs.

contacts (22.7%) indicate efficient close packing, while H···F/F···H contacts (12.7%) and other heteroatom-involving contacts such as C···N/N···C (7.9%) and N···N (6.3%) further enrich the secondary interaction network. The presence of multiple, spatially distributed short contacts (including hydrogen bonds and ancillary heteroatom contacts) is expected to facilitate stress delocalization under mechanical stimuli, consistent with the experimentally observed insensitivity of **4**. For **5**, the Hirshfeld surface mapped over *d*_norm (Fig. 5) shows multiple intense red spots concentrated around the protonated N–H donors and the oxygen atoms of the NO_3^- anion, evidencing strong and highly directional N–H···O hydrogen-bonding interactions; additional short-contact features are also distributed near ring nitrogens, consistent with auxiliary N–H···N contacts. Quantitatively, the 2D fingerprint plots confirm that hydrogen-bond-related interactions dominate lattice cohesion: N···H/H···N contacts contribute 26.5% and O···H/H···O contacts contribute 13.2%, giving a combined 39.7% of the total surface contacts. Beyond these primary hydrogen bonds, H···F/F···H contacts (22.4%) are prominent, reflecting close approaches between the CF_3 groups and surrounding hydrogen donors, while H···H contacts (13.4%) indicate efficient close packing. The remaining 24.5% ("Others") corresponds to a range of weaker secondary contacts that further consolidate the solid-state network. Overall, the dense, spatially distributed short contacts in **5**—dominated by N–H···O/N–H···N interactions and supplemented by H···F and packing contacts—are expected to promote stress delocalization under mechanical stimuli, consistent with the experimentally observed low sensitivity of **5**.

Complementary ESP analyses further support this interpretation. For neutral **3**, the surface potential spans from V_s, min = −49.31 to V_s, max = +45.03 kcal mol^{-1}, a moderate range of ~94.34 kcal mol^{-1} with a balanced distribution. Upon perchlorate salt formation, **[3H]**$^+$ exhibits an expanded high-potential window (22.67 to 121.46 kcal mol^{-1} on the mapped surface), reflecting the ionic character introduced by protonation and ClO_4^- pairing. Importantly, although **[3H]**$^+$ shows higher extreme surface potentials, its overall potential dispersion is similar to that of **3**, suggesting a broadly distributed electrostatic surface rather than a highly localized one. Combined with the extensive N–H···O interactions evidenced by HS analysis, this feature provides a plausible microscopic basis for the preserved low sensitivity of **[3H]**$^+$. Meanwhile, salt formation can introduce additional initiation pathways because oxygen-rich anions and hydrogen-bonded ion pairs are more susceptible to early-stage reactions than the neutral framework. Overall, ionization strengthens lattice interactions and improves energetic performance, while altering thermal-decomposition kinetics *via* anion-assisted activation (Fig. 6).

Conclusions

In summary, a series of CF_3-functionalized, triazine-linked nitrogen-rich energetic compounds (**3–6**) were constructed through an SNAr-based modular strategy from a chlorotriazine core and a fused 5/5 triazolo[4,3-*b*][1,2,4]triazole precursor. Relative to precursor **2** (T_d = 215 °C), incorporation of the triazine unit increases the decomposition threshold of this framework, with compound **3** showing the highest onset decomposition temperature in the present series (T_d = 253 °C). Subsequent ionic modulation further tunes density and energetic output: perchlorate salt **4** reaches a density of 1.80 g cm^{-3} and delivers D = 7664 m s^{-1} and P = 25.2 GPa, whereas nitrate salt **5** shows intermediate performance (D = 7228 m s^{-1}, P = 20.8 GPa). By contrast, the triazine-bridged dimer **6** retains very low mechanical sensitivity but exhibits comparatively lower density, detonation output, and thermal stability within this series (T_d = 234 °C). Notably, all four compounds remain highly

insensitive toward impact and friction (IS > 40 J, FS > 360 N). Overall, these results indicate that triazine bridging combined with ionic modulation provides a useful strategy for tuning the balance among thermal behaviour, detonation performance, and low mechanical sensitivity in CF_3-containing nitrogen-rich frameworks, with perchlorate salt **4** showing the most balanced overall combination of energetic performance and insensitivity.

Author contributions

Jiyuan Yu: investigation, data curation, writing – original draft. Xiangyan Miao: methodology, writing – review & editing. Yuchuan Li: conceptualization, supervision, funding acquisition, writing – review & editing.

Conflicts of interest

There are no conflicts to declare.

Data availability

CCDC 2525729 and 2530986 contain the supplementary crystallographic data for this paper.[33a,b]

The data underlying this study are available in the published article and its supporting information (SI). Supplementary information is available. See DOI: https://doi.org/10.1039/d6ra01290f.

Acknowledgements

This work was supported by the National Natural Science Foundation of China [No. 22135003].

Notes and references

1 X. Miao, J. Yu, Y. Li and S. Pang, Constructing nitrogen-rich fused [5,6,5]-tricyclic frameworks through rearrangement: heat-resistant zwitterionic salt energetic materials, *Org. Lett.*, 2024, **26**, 10085–10089.
2 J. Cai, C. Xie, J. Xiong, J. Zhang, P. Yin and S. Pang, High performance and heat-resistant pyrazole-1,2,4-triazole energetic materials: tuning the thermal stability by asymmetric framework and azo-bistriazole bridge, *Chem. Eng. J.*, 2022, **433**, 134480.
3 Q. Sun, Z. Jiang, N. Ding, C. Zhao, B. Tian, S. Li and S. Pang, Assembly of three oxadiazole isomers toward versatile energetics, *J. Mater. Chem. A*, 2023, **11**, 23228–23232.
4 H. Zhang, J. Cai, Z. Li, Q. Lai, P. Yin and S. Pang, Exploring a Fused Triazole–Tetrazine Binary CN Material for a Promising Initiating Substance, *ACS Appl. Mater. Interfaces*, 2024, **16**, 4628–4636.
5 A. K. Sikder and N. Sikder, A review of advanced high performance, insensitive and thermally stable energetic materials emerging for military and space applications, *J. Hazard. Mater.*, 2004, **112**, 1–15.
6 R. P. Singh, R. D. Verma, D. T. Meshri and J. M. Shreeve, Energetic nitrogen-rich salts and ionic liquids, Angew, *Chem., Int. Ed.*, 2006, **45**, 3584–3601.
7 T. M. Klapötke, J. Stierstorfer, M. Weyrauther and T. G. Witkowski, Synthesis and investigation of 2,6-bis(picrylamino)-3,5-dinitropyridine (PYX) and its salts, *Chem. Eur. J.*, 2016, **22**, 8619–8626.
8 X. Miao, J. Yu, S. Jiang, Y. Li and S. Pang, Reactivity investigation of bis-tetrazole isomers prepared through Dimroth rearrangement, *Org. Lett.*, 2026, **28**, 929–934.
9 H. Gao, Q. Zhang and J. M. Shreeve, Fused heterocycle-based energetic materials (2012–2019), *J. Mater. Chem. A*, 2020, **8**, 4193–4216.
10 S. Chen, W. Zhang, Y. Wang and Q. Zhang, [1,2,4]Triazolo[4,3-b]pyridazine as a building block towards low-sensitivity high-energy materials, *Chem. Eng. J.*, 2021, **421**, 129635.
11 P. Yin, C. He and J. M. Shreeve, Fused heterocycle-based energetic salts: alliance of pyrazole and 1,2,3-triazole, *J. Mater. Chem. A*, 2016, **4**, 1514–1519.
12 J. Zhang, Y. Feng, R. J. Staples, J. Zhang and J. M. Shreeve, Taming nitroformate through encapsulation with nitrogen-rich hydrogen-bonded organic frameworks, *Nat. Commun.*, 2021, **12**, 2146.
13 M. S. Gruhne, M. Lommel, M. H. H. Wurzenberger, T. M. Klapötke and J. Stierstorfer, Investigation of ethylenedinitramine as a versatile building block in energetic salts, cocrystals, and coordination compounds, *Inorg. Chem.*, 2021, **60**, 4816–4828.
14 Z. Yan, T. Lu, Y. Liu, W. Liu, B. Zhao, Y. Wang and Z. Ge, High thermal stability and insensitive fused triazole–triazine trifluoromethyl-containing explosives (TFX), *ACS Omega*, 2021, **6**, 18591–18597.
15 Y. Kang, Y. Dong, Y. Liu, H. Gao, Y. Wang and J. M. Shreeve, Halogen bonding (C–F···X) and its effect on creating ideal insensitive energetic materials, *Chem. Eng. J.*, 2022, **440**, 135969.
16 S. Nehe, A. K. Yadav, V. D. Ghule and S. Dharavath, Employing the Trifluoromethyl Group on a 5/5 Fused Triazolo[4,3-b][1,2,4]triazole Backbone: A Viable Strategy for Attaining Balanced Energetics, *Org. Lett.*, 2024, **26**, 10611–10615.
17 P. Xie, X. Liao and J. Liu, Ignition and combustion characteristics of aluminum-based fluorine-containing composite powder, *Thermochim. Acta*, 2024, **736**, 179757.
18 Q. Sun, W. Chen, N. Ding, C. Zhao, Z. Jiang, S. Li and S. Pang, Unraveling the direct effect of hydrogen bonding on density and thermostability of energetic materials through isomerism, *Chem. Eng. J.*, 2022, **444**, 136539.
19 X. Jiang, D. Yin, S. Song, Y. Wang, M. Fan, R. Wang and Q. Zhang, Achieving ultra-high heat resistance of novel energetic materials through a hydrogen bonding and extended π-conjugation strategy, *J. Mater. Chem. A*, 2024, **12**, 13231–13239.
20 J. Ma, Y. Tang, G. Cheng, G. H. Imler, D. A. Parrish and J. M. Shreeve, Energetic derivatives of 8-nitropyrazolo[1,5-a][1,3,5]triazine-2,4,7-triamine: achieving balanced explosives

by fusing pyrazole with triazine, *Org. Lett.*, 2020, **22**, 1321–1325.
21 X. Jiang, R. Wang, M. Fan, S. Song, Y. Wang and Q. Zhang, Combination of 5-amino-4-nitro-1,2-dihydro-3H-pyrazol-3-one and azine frameworks for insensitive, heat-resistant energetic materials, *Dalton Trans.*, 2025, **54**, 7056–7061.
22 W. Ma, J. Li, C. He and S. Pang, Synthesis of two series of isomeric triazolo-triazine fused energetic salts: high thermal stability, insensitivity, and high performances, *Cryst. Growth Des.*, 2023, **23**, 3463–3470.
23 J. Ma, G. Cheng, X. Ju, Z. Yi, S. Zhu, Z. Zhang and H. Yang, Amino-nitramino functionalized triazolotriazines: a good balance between high energy and low sensitivity, *Dalton Trans.*, 2018, **47**, 14483–14490.
24 S. Kronister, D. Svatunek, C. Denk and H. Mikula, Acylation-mediated 'kinetic turn-on' of 3-amino-1,2,4,5-tetrazines, *Synlett*, 2018, **29**, 1297–1302.
25 W. N. Carson, J. W. Vanderwater and H. S. Gile, Coulometric determination of plutonium, *Anal. Chem.*, 1957, **29**, 1417–1422.
26 T. Ozawa, Kinetics in differential thermal analysis, *Bull. Chem. Soc. Jpn.*, 1965, **38**, 1881–1886.
27 M. Sućeska, *Explo5 (Version 6.05), OZM Research s.r.o., Pardubice*, 2018.
28 P. Richardson, A. A. Kitos, M. Triglav, J. S. Ovens, I. Laroche, S. Delisle, B. Jolicoeur, J. L. Brusso and M. Murugesu, Synthesis and detonation performance of novel tetrazolyl–triazine nitrogen-rich energetic materials, *Mater. Adv.*, 2023, **4**, 5775–5784.
29 H. Gao, Q. Zhang and J. M. Shreeve, Fused heterocyclebased energetic materials (2012–2019), *J. Mater. Chem. A*, 2020, **8**, 4193–4216.
30 T. Lu and F. Chen, Multiwfn: a multifunctional wavefunction analyzer, *J. Comput. Chem.*, 2012, **33**, 580–592.
31 W. Humphrey, A. Dalke and K. Schulten, VMD: visual molecular dynamics, *J. Mol. Graphics*, 1996, **14**, 33–38.
32 P. R. Spackman, M. J. Turner, J. J. McKinnon, S. K. Wolff, D. J. Grimwood, D. Jayatilaka and M. A. Spackman, CrystalExplorer: a program for Hirshfeld surface analysis, visualization and quantitative analysis of molecular crystals, *J. Appl. Crystallogr.*, 2021, **54**, 1006–1011.
33 (*a*) CCDC 2525729: Experimental Crystal Structure Determination, 2026, DOI: 10.5517/ccdc.csd.cc2qs74x; (*b*) CCDC 2530986: Experimental Crystal Structure Determination, 2026, DOI: 10.5517/ccdc.csd.cc2qypq3.